Research Square

Preprints are preliminary reports that have not undergone peer review.
They should not be considered conclusive, used to inform clinical practice,
or referenced by the media as validated information.

Analytical Subdomain Modeling of an H-Type Switched Reluctance Machine with Circumferential Cross-Winding Considering Magnetic Saturation for Reluctance Torque and unbalanced magnetic force Prediction

E. Shirzad

dr.ehsan.shirzad@tooranihe.ac.ir

Tooran Institute of Higher Education

Research Article

Keywords:

Posted Date: November 9th, 2026

DOI: https://doi.org/10.21203/rs.3.rs-11247858/v1

License: This work is licensed under a Creative Commons Attribution 4.0 International License.
Read Full License

Additional Declarations: No competing interests reported.

Analytical Subdomain Modeling of an H-Type Switched Reluctance Machine with Circumferential Cross-Winding Considering Magnetic Saturation for Reluctance Torque and unbalanced magnetic force Prediction

E.Shirzad

Faculty of Electrical Engineering, Tooran Institute of Higher Education, Damghan, Iran

*Correspondence: dr.ehsan.shirzad@tooranihe.ac.ir

Abstract— Switched reluctance machines (SRMs) are valued for their rugged, magnet-free construction, yet their doubly salient geometry makes accurate electromagnetic modeling a persistent challenge, particularly under deep saturation, where linear analytical approaches lose fidelity. This work develops a two-dimensional analytical subdomain model for an H-Type SRM equipped with a circumferential cross-winding arrangement, in which each slot accommodates a single circumferential coil wound around the H-bridge, forming a cross-magneto motive force (MMF) distribution that shapes the airgap field in a distinctive manner. The machine geometry is partitioned into rotor yoke, rotor teeth, airgap, stator slots, stator teeth, and stator yoke, with Maxwell's equations solved analytically in each region. To capture the nonlinear behavior of the iron core, an iterative two-component saturation correction is embedded into the model, applying local adjustments to both radial and tangential flux density components in the stator teeth, rotor teeth, and yoke based on the measured B–H characteristic of the lamination steel. From the corrected field solution, the electromagnetic torque and unbalanced magnetic force (UMF) are derived. Finite element simulations are used to validate the analytical predictions, and the results confirm the model's ability to reproduce the field distribution and integral quantities with good accuracy. The proposed framework offers a computationally efficient tool for the analysis of H-Type SRM topologies, with particular relevance to applications where UMF and electromagnetic torque must be predicted reliably, such as in-wheel traction drives and high-speed actuator systems.

***Index Terms*— Analytical modeling, H-Type SRM, circumferential cross-winding, magnetic saturation, subdomain method, UMF.**

MAIN SYMBOLS

$\boldsymbol{A}$	Magnetic vector potential (V.s/m)
$\boldsymbol{B}$	Magnetic flux density vector (T)
$\boldsymbol{H}$	Magnetic field intensity vector (A/m)
$\boldsymbol{J}$	Armature current density vector (A/m^2)
$\boldsymbol{M}$	Magnetization vector (A/m).
μ_0	Free space permeability (H/m).
μ_r	Relative permeability
N_{ss}	Number of stator slots
N_{irs}	Number of inner rotor slots
N_{ors}	Number of outer rotor slots
α_i	Central angle of *i*th slot of inner rotor
β_i	Central angle of *i*th slot of inner stator
σ_i	Central angle of *i*th slot of outer rotor
λ_i	Central angle of *i*th slot of outer stator
$\boldsymbol{F}_x$	Total x-direction force exerted on rotor (N)
$\boldsymbol{F}_y$	Total y-direction force exerted on rotor (N)
$\boldsymbol{T}_{ele}$	Reluctance torque (N.m)
n,m,v,u,h	Harmonic order

Superscripts and subscripts

r	Radial direction
k	Iterative coefficient
θ	Tangential direction
z	Axial direction
iry	Inner rotor yoke
irs	Inner rotor slot
ia	Inner airgap
ss	stator slot
i	Rank of tooth
oa	Outer airgap
ors	Outer rotor slot
ory	Outer rotor yoke
iss	inner stator slot
oss	Outer stator slot
$\boldsymbol{B}_r$	Radial flux density
$\boldsymbol{B}_\theta$	Tangential flux density

I. INTRODUCTION

SRMs have attracted considerable attention in recent years owing to their simple and cost-effective construction, high mechanical and thermal robustness, wide speed range, and excellent reliability. These features make them particularly suitable for harsh operating conditions and position them as strong candidates for next-generation drive systems. SRMs have already been successfully employed in a variety of applications, including electric vehicles, mining machinery, and aircraft [1–3].

Motivated by these advantages, extensive research has been devoted to the modeling and design of SRMs. A wide spectrum of techniques has been developed to improve their performance, ranging from numerical methods to various analytical approaches. In parallel, many studies have concentrated on alternative machine structures, including modifications to the motor geometry and different winding arrangements. For instance, [4] analyzes a double-sided linear switched reluctance motor (DSLS-RM) equipped with an auxiliary winding for ropeless elevators. Linear switched reluctance motors are generally classified, based on their structure, into single-sided and double-sided types. In [5], the selection of the stator pole tip is investigated as a means of mitigating torque ripple, where electromagnetic analysis and simulation are used to evaluate the influence of pole-tip variation on ripple reduction. Reference [6] presents a

comparative study of eight winding configurations in a four-phase 16/12 SRM, examining their effects on developed torque, power, efficiency, and inductance.

Several studies have focused on analytical and mathematical modeling of SRMs under different operating conditions. In [7], a model of the motor winding current is derived for the elimination of braking force, and the proposed model is validated in MATLAB/Simulink using typical motor characteristics. Reference [8] establishes a mathematical model for a 12/14 hybrid stator-pole bearingless SRM by redesigning the traditional integral path based on the Maxwell stress tensor method, enabling accurate calculation of levitation force and torque over a complete period. From a structural perspective, [9] proposes a new seven-phase, yokeless, double-rotor SRM with flux paths between adjacent stator teeth. By exploiting self and mutual inductances between windings, this topology increases both torque and power density while reducing torque pulsation. In [10], a 12/14 bearingless SRM with hybrid stator poles is proposed to achieve high output torque density and excellent decoupling between torque and suspension force. Reference [11] presents a design methodology and optimization of a 20/16 outer-rotor five-phase SRM (OR-FPSRM) for in-wheel drive applications, in which an analytical model is derived to estimate the static torque. Vibration and acoustic behavior have also received attention. Reference [12] conducts FEM-based electromagnetic and mechanical analysis on a three-phase, 1 kW, 48 V, 3000 rpm SRM prototype, beginning with modal analysis of the stator, rotor, shaft, and frame to identify the dominant natural vibration modes. In [13], a novel design method is proposed for a 12-pole, 20-slot, five-phase multi-mode reluctance motor (MRM) to balance the performance of both the synchronous reluctance motor (SynRM) mode and the SRM mode across the entire speed range. Analytical modeling under saturation remains a central research theme. Reference [14] introduces a "switched lumped reluctance network" equivalent circuit for an SRM under saturation, incorporating the effects of position-dependent phase switching and rotor movement. In [15], a novel design theory based on nonlinear characteristics is proposed, in which speed–torque requirements and control methods are embedded into a nonlinear flux-linkage model. Reference [16] investigates the use of phase currents to eliminate torque and input-current ripples, addressing the difficulties encountered under magnetic saturation. Further contributions address hybrid modeling, fault diagnosis, and magnetic equivalent circuits. Reference [17] proposes a geometry-dependent hybrid model for a higher-phase SRM that accounts for mutual coupling and core saturation, with minimal reliance on FEA and significantly reduced computation time. In [18], the magnetic behavior of SRMs under inter-turn fault conditions is examined through detailed FEA supported by experimental validation, focusing on flux linkage, inductance, and electromagnetic torque. Reference [19] develops a reluctance mesh-based magnetic equivalent circuit (MEC) model for three-phase 6/4, 6/16, and 12/8 SRMs as well as four-phase 8/6, 8/10, and 16/12 SRMs, comparing static and dynamic characteristics with FEM and experimental results. Additional studies target linear and bearingless topologies. To accurately estimate the dynamic performance of a linear SRM with segmented secondary, [20] develops a nonlinear inductance function (NIF) that accounts for iron saturation effects. In [21], a mathematical model considering magnetic saturation is proposed for a 12/4 bearingless SRM, in which levitation forces are generated in the maximum-inductance flat region of each phase. Finally, drive and identification aspects are covered in [22]–[26]. Reference [22] presents a new power converter topology enabling reconfigurable winding operation in a double-stator axial-flux SRM (DSAFSRM). In [23], a dynamic model of a 6/8 external-rotor SRM (ER-SRM) is developed in MATLAB/Simulink, with magnetic characteristics obtained via FEM. Reference [24] proposes an accurate and fast analytical approach for determining the phase inductance of a single-tooth winding segmental-rotor SRM at any rotor position. Reference [25] investigates the harmonic content and torque generation mechanism of reluctance-type machines using air-gap field modulation theory. Lastly, [26] proposes a robust method for SRM modeling and parameter identification based on the Hammerstein approach and frequency response analysis, validated against FEA and recursive least squares (RLS).Although conventional SRM topologies offer a rugged and magnet-free structure, their doubly salient geometry introduces several well-known drawbacks. As illustrated in Fig. 1, the conventional arrangement suffers from a highly non-uniform airgap field, pronounced flux crowding at the stator and rotor pole tips, and a strong tendency toward deep local saturation, particularly in the stator teeth and yoke. These effects lead to inaccurate prediction of key electromagnetic quantities when linear analytical models are employed, and they also contribute to elevated torque ripple, acoustic noise, and unbalanced magnetic force (UMF). Moreover, the absence of a structured magneto motive force (MMF) distribution in the airgap makes it difficult to shape the field in a controlled manner, which limits the achievable torque density and complicates the design of high-performance drive systems such as in-wheel traction motors and high-speed actuators. More importantly, a review of the existing literature reveals that no analytical model has yet been reported for this class of machines that simultaneously accounts for the saturation effect in both the radial and tangential components of the flux density. This gap is particularly significant because, under deep saturation, the tangential component plays a non-negligible role in torque production and UMF, and neglecting it leads to considerable inaccuracy in the predicted electromagnetic performance. To address these limitations, an H-Type SRM with a single-layer circumferential cross-winding arrangement is proposed, as shown in Fig. 2. The H-Type concept, originally introduced in [27], is adapted here to a switched reluctance topology. In this arrangement, each slot accommodates a single circumferential coil wound around the H-bridge, and the coils of adjacent slots are connected MMF distribution that shapes the airgap field in a distinctive and more controllable manner, without increasing the number of coils per slot. Unlike the conventional single-tooth winding, in which the end winding runs parallel to the direction of motion and the slot leakage opposes the main flux path, the circumferential winding ensures that the slot leakage does not

link the coil, thereby improving the net flux linkage and the resulting force capability. To capture the nonlinear behavior of the iron core, an iterative two-component saturation correction is embedded into the model, applying local adjustments to both radial and tangential flux density components in the stator teeth, rotor teeth, and yoke based on the measured B–H characteristic of the lamination steel. From the corrected field solution, the electromagnetic torque and UMF are derived. Finite element simulations are used to validate the analytical predictions, and the results confirm the model's ability to reproduce both the field distribution and the integral quantities with good accuracy. The proposed framework therefore offers a computationally efficient tool for the analysis of H-Type SRM topologies, with particular relevance to applications where UMF and electromagnetic torque.

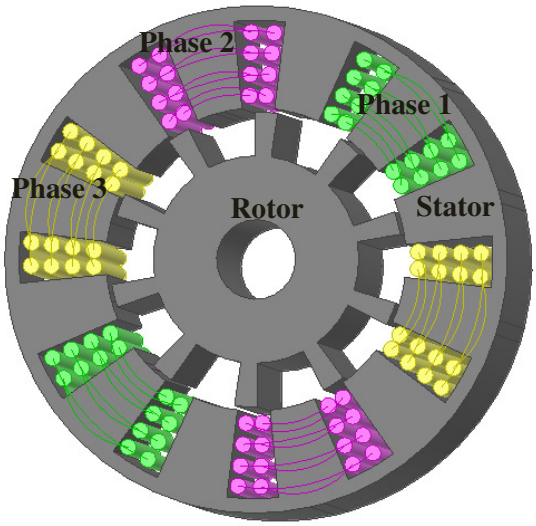


Figure 1. Conventional SRM with single layer layout of winding

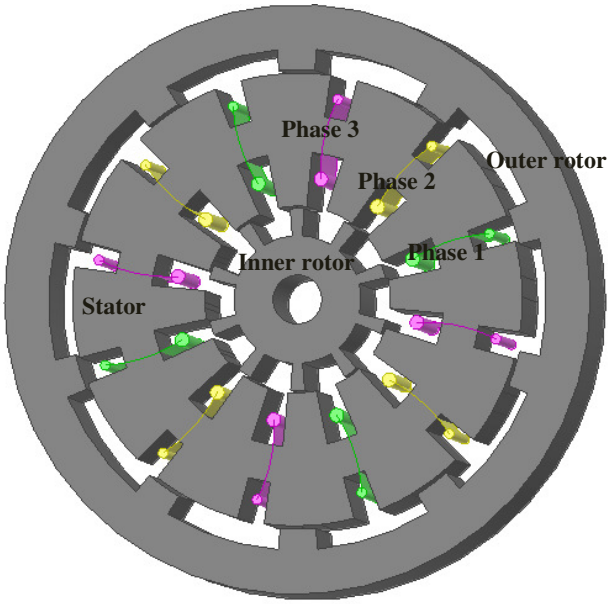


Figure 2. Proposed H-type SRM with single layer layout of winding and two-rotor single sandwiched stator

II. ANALYTICAL MODEL

This section outlines the analytical framework used to predict the electromagnetic behavior of the proposed H-Type SRM. The modeling approach adopts the subdomain method, which provides closed-form solutions for the magnetic field distribution by solving Maxwell's equations independently within each region of the machine. In this analytical model, the iron permeability is initially assumed infinite, but under high load, saturation occurs and this assumption fails. An iterative two-component saturation correction is therefore applied to overcome this problem.

The main benefit of this technique lies in its computational efficiency compared to finite element analysis, while still delivering acceptable accuracy for design and optimization studies.

Figure 3 shows the division of the machine cross-section into distinct subdomains, each defined by specific material properties and source terms. Unlike conventional SRMs, the proposed H-Type topology features two airgaps (inner and outer) and two sets of rotor slots (inner and outer), which significantly influence the field distribution. The iron regions, including the stator teeth (inner and outer), the H-bridge, and the yokes, are assumed to have infinite permeability in the linear solution, meaning that the magnetic field intensity $\boldsymbol{H}$ is zero within these regions.

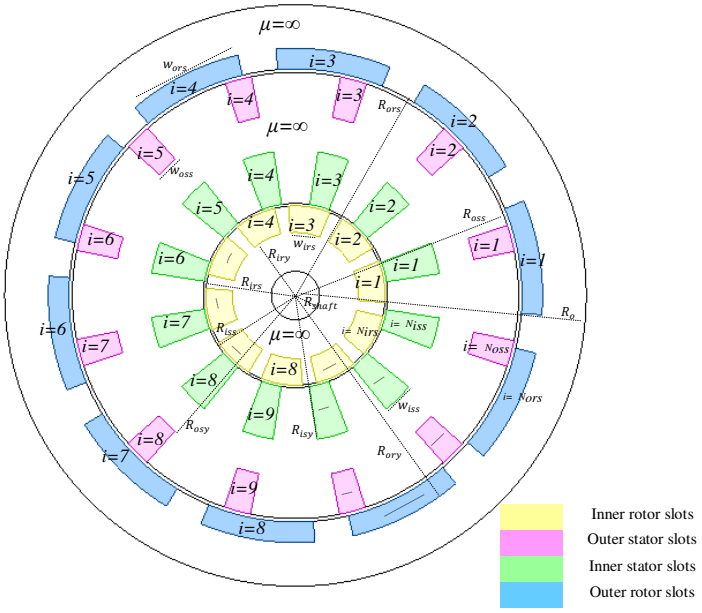


Figure 3. Distinct regions and geometry of H-type SRM for linear analytical model

The subdomains are classified into two categories:

Non-magnetic regions (where Maxwell's equations are solved):

Inner rotor slot (*irs*), Outer rotor slot (*ors*), Inner airgap (*ia*), Outer airgap (*oa*), Inner and outer stator slot containing the circumferential winding (*irs, ors*).

Iron regions (where $\mu=\infty$ and $\boldsymbol{H}=0$):

Inner stator tooth (*ist*), Outer stator tooth (*ost*), Stator yoke (*sy*), Rotor yoke (*ry*) and H-bridge.

For each non-magnetic region, the appropriate governing equation is selected based on whether current sources are present. Since the H-Type SRM contains no permanent magnets, the magnetization vector $\boldsymbol{M}$ is zero in all regions, and the only source term is the current density $\boldsymbol{J}$ in the stator slot.

A. Problem Formulation

The magnetic field within the machine is described using the magnetic vector potential $\boldsymbol{A}$, which satisfies the following general equation in each subdomain:

$$-\nabla^2 A_z^i = \mu_0 \mu_r J_z^i + \frac{\mu_0}{r}\left(\frac{\partial M_r}{\partial \theta} - r\frac{\partial M_\theta}{\partial r}\right) \tag{1}$$

Since the H-Type SRM is a magnet-free machine, the magnetization term is zero in all regions ($M_r=M_\theta=0$). Therefore, equation (1) simplifies to:

$$-\nabla^2 A_z^i = \mu_0 \mu_r J_z^i \tag{2}$$

In non-magnetic regions without any current sources (inner rotor slot, outer rotor slot, inner airgap, and outer airgap), equation (2) reduces to Laplace's form:

$$\nabla^2 A_z^i = 0 \tag{3}$$

In the stator slot region, where the circumferential winding carries current, Poisson's equation applies with J_z^i acting as the source term:

$$-\nabla^2 A_z^i = \mu_0 \mu_r J_z^i \tag{4}$$

In the iron regions, since the permeability is assumed infinite, the magnetic field intensity is zero ($\boldsymbol{H}=0$), and the magnetic vector potential is constant. Therefore, no differential equation is solved in these regions; instead, the boundary conditions at the interfaces between iron and non-magnetic regions are enforced.

The flux density components are obtained from $\boldsymbol{B}= \boldsymbol{\nabla}\times\boldsymbol{A}$:

$$B_r = \frac{1}{r}\frac{\partial A_Z}{\partial \theta} \tag{5}$$

$$B_\theta = -\frac{\partial A_Z}{\partial r} \tag{6}$$

The magnetic field intensity in the non-magnetic regions is calculated as:

$$\boldsymbol{H} = \frac{\boldsymbol{B}}{\mu_0} \tag{7}$$

B. General Solutions in Each Subdomain

1. Inner and outer Rotor Slot (Non-Magnetic Region – Laplace's Equation)

The inner rotor slot is a passive region located between the inner airgap and the rotor yoke. Since this region contains no current sources, the field is governed by Laplace's equation. For each inner rotor slot ii, with central angle $\alpha_i$and slot width w_{irs}, Similarly, for each outer rotor slot *i*, with central angle λ_i and slot width w_{ors} :

The general solution is expressed as a Fourier cosine series:

$$\mathrm{A_z^i}(r,\theta) = a_{i,0} + \sum_{m=1}^{\infty}\left(\left(a_{\mathrm{i,m}} r^{\frac{m\pi}{w_{irs}}} + b_{\mathrm{i,m}} r^{\frac{-m\pi}{w_{irs}}}\right)\cos\left(\frac{\mathrm{m\pi}}{w_{irs}}\left(\theta - \alpha_{\mathrm{i}} + \frac{w_{irs}}{2}\right)\right)\right) \tag{8}$$

$$\mathrm{A_z^i}(r,\theta) = a_{i,0} + \sum_{h=1}^{\infty}\left(\left(a_{\mathrm{i,h}} r^{\frac{h\pi}{w_{ors}}} + b_{\mathrm{i,h}} r^{\frac{-h\pi}{w_{ors}}}\right)\cos\left(\frac{\mathrm{h\pi}}{w_{ors}}\left(\theta - \lambda_{\mathrm{i}} + \frac{w_{ors}}{2}\right)\right)\right) \tag{9}$$

2. Inner and outer Airgap (Non-Magnetic Region – Laplace's Equation)

The inner airgap is located between the inner rotor slot and the inner stator tooth. The solution includes both cosine and sine terms to cover the full circumferential span:

$$\mathrm{A_z^i}(r,\theta) = \sum_{n=1}^{\infty}((a_{1n}(r)^n + a_{2n}(r)^{-n})cos(n\theta) + (b_{1n}(r)^n + b(r)^{-n})sin(n\theta) \tag{10}$$

3. Inner and outer stator Slot (Non-Magnetic Region – Poisson's Equation with Current Source)

In the stator slot that carries the circumferential winding current, the solution consists of a general solution to the homogeneous equation plus a particular solution that accounts for the current density. For the inner stator slot, with central angle β_i and slot width w_{iss} and outer slot, with central angle σ_i and slot width w_{oss} :

$$A_z^i(r,\theta) = a_{i,0} + b_{i,0}ln(r) - \frac{1}{4}\mu_0 J_i r^2 + \sum_{u=1}^{\infty}\left((a_{iu}\, r^{\frac{-u\pi}{w_{iss}}} + b_{i,u} r^{\frac{u\pi}{w_{iss}}})cos\,(\frac{u\pi}{w_{iss}}\left(\theta - \beta_i + \frac{w_{iss}}{2}\right)\right) \quad (11)$$

$$J_i(\theta) = J_{i,0} + \sum_{u=1}^{\infty}\left(J_{i,u}\, cos\,(\frac{u\pi}{w_{iss}}\left(\theta - \sigma_i + \frac{w_{iss}}{2}\right)\right) \quad (12)$$

$$A_z^i(r,\theta) = a_{i,0} + b_{i,0}ln(r) - \frac{1}{4}\mu_0 J_i r^2 + \sum_{v=1}^{\infty}\left((a_{iv}\, r^{\frac{-v\pi}{w_{oss}}} + b_{i,v} r^{\frac{v\pi}{w_{oss}}})cos\,(\frac{v\pi}{w_{oss}}\left(\theta - \sigma_i + \frac{w_{oss}}{2}\right)\right) \quad (13)$$

$$J_i(\theta) = J_{i,0} + \sum_{v=1}^{\infty}\left(J_{i,v}\, cos\,(\frac{v\pi}{c}\left(\theta - \sigma_i + \frac{w_{oss}}{2}\right)\right) \quad (14)$$

4. Iron Regions (Infinite Permeability)

In the inner stator tooth, outer stator tooth, stator yoke, H-bridge, and rotor yoke, the permeability is assumed infinite in the linear solution. Consequently, the magnetic field intensity is zero within these regions (Figure4):

$$\boldsymbol{H} = 0, \boldsymbol{A}_z = \text{constant}$$

No differential equation is solved in these regions. Instead, the boundary conditions at the interfaces between the iron regions and the adjacent non-magnetic regions are enforced.

C. Boundary Conditions

The unknown coefficients in the general solutions are determined by applying appropriate boundary conditions at the interfaces between adjacent subdomains. At each interface, two physical conditions must be satisfied:

1. **Continuity of the magnetic vector potential A_z^i:**

$$A_z^{First\ region}\left(R_{interface},\theta\right) = A_z^{Second\ region}\left(R_{interface},\theta\right) \quad (15)$$

2. **Continuity of the tangential component (may be in tangential or radial direction) of the magnetic field intensity *H*:**

$$H_{\theta,r}^{First\ region}\left(R_{interface},\theta\right) = H_{\theta,r}^{Second\ region}\left(R_{interface},\theta\right) \quad (16)$$

This condition is applied at the following interfaces:

- Inner rotor slot – inner stator tooth (through the inner airgap)
- Outer rotor slot – outer stator tooth (through the outer airgap)
- Inner airgap – inner stator tooth
- Outer airgap – outer stator tooth
- Stator slot – stator yoke / H-bridge

These conditions are enforced through Fourier projection, yielding a system of linear equations that can be solved efficiently.

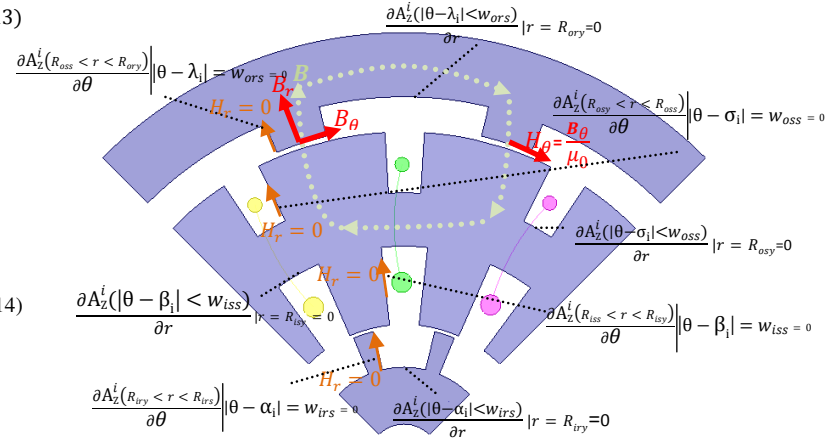


Figure 4. Boundary conditions with respect to infinite permeability of iron

D. Two-Component Saturation Correction

The linear solution obtained from the subdomain method assumes infinite permeability in the iron core. While this assumption provides a reasonable first approximation, it fails to capture magnetic saturation effects under high-load conditions, where the flux density in the teeth and yoke exceeds the knee point of the *B–H* curve. To address this limitation, an iterative saturation correction procedure is developed that accounts for both radial and tangential flux density components.

1. Flux Calculation in Teeth and Yoke Regions

For each stator and rotor tooth *i* (inner or outer), the flux is obtained by integrating the radial component of the flux density over the tooth pitch at the mean radius of the tooth, where L_s is depth of machine:

$$\phi_{i,tooth}^{inner\ stator} = R_{iss}.L_s\int_{\beta_{i-1}+w_{iss}/2}^{\beta_i - w_{iss}/2} B_{r,linear}^{inner\ airgap}\, d\theta \quad (17)$$

$$\phi_{i,tooth}^{outer\ stator} = R_{oss}.L_s\int_{\sigma_{i-1}+w_{oss}/2}^{\sigma_i - w_{oss}/2} B_{r,linear}^{outer\ airgap}\, d\theta \quad (18)$$

$$\phi_{i,tooth}^{inner\ rotor} = R_{irs}.L_s \int_{\alpha_{i-1}+w_{iss}/2}^{\alpha_i - w_{iss}/2} B_{r,linear}^{inner\ airgap} d\theta \quad (19)$$

$$\phi_{i,tooth}^{outer\ rotor} = R_{ors}.L_s \int_{\lambda_{i-1}+w_{oss}/2}^{\lambda_i - w_{oss}/2} B_{r,linear}^{outer\ airgap} d\theta \quad (20)$$

For the yoke regions, the flux is computed by dividing the sum of the tooth fluxes by the number of yoke segments between adjacent teeth as shown in Figure5:

$$\phi_{yoke,i}^{inner\ rotor} = \frac{2}{N_{irs}} \sum_{i=1}^{N_{irs}} \phi_{i,tooth}^{inner\ rotor} \quad (21)$$

$$\phi_{yoke,i}^{outer\ rotor} = \frac{2}{N_{ors}} \sum_{i=1}^{N_{ors}} \phi_{i,tooth}^{outer\ rotor} \quad (22)$$

$$\phi_{yoke,i}^{stator} = \frac{2}{N_{ss}} \sum_{i=1}^{N_{ss}} \phi_{i,tooth}^{inner\ stator} + \frac{2}{N_{ss}} \sum_{i=1}^{N_{ss}} \phi_{i,tooth}^{outer\ stator} \quad (23)$$

Where $N_{yoke}$is the number of yoke segments between two adjacent teeth.

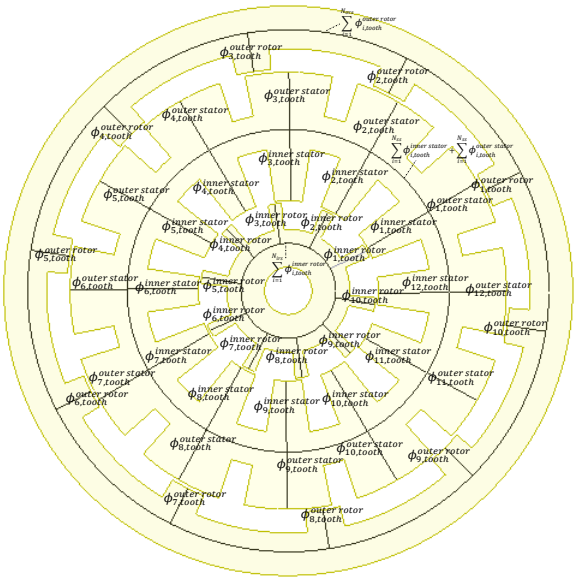


Figure 5. Path of flux all over the machine

2. Flux Density in Each Iron Region

From the calculated fluxes, the average flux density in each iron region is determined by dividing the flux by the effective cross-sectional area. Equations (24) to (30) determine the average flux density in each iron region by dividing the total flux passing through that region by its effective cross-sectional area. For the inner and outer stator teeth, equations (24) and (25) express the radial flux density in terms of the tooth flux, the stack length, the tooth width, and the mean radius of the tooth, while equations (27) and (28) apply the same formulation to the inner and outer rotor teeth. For the yoke regions, equations (26), (29), and (30) compute the flux density by dividing the yoke flux by the effective yoke cross-sectional area, defined as the stack length multiplied by the radial thickness of the corresponding yoke. Equations (31) to (34), in turn, determine the tangential component of the flux density in the teeth by enforcing the continuity of the tangential magnetic field intensity H_θ at the iron–air interface. Owing to this continuity, the tangential flux density in each tooth is obtained by dividing the tangential flux density in the adjacent airgap by the local relative permeability of that tooth; equations (31) and (32) apply this relation to the inner and outer stator teeth, respectively, while equations (33) and (34) apply it to the inner and outer rotor teeth. In each case, the numerator is derived from the analytical solution of the corresponding airgap, whereas the denominator is the local relative permeability of the tooth, which is updated iteratively during the saturation correction procedure. As saturation increases and μ_r decreases, the tangential component $B_{\theta,\text{tooth}}$ becomes increasingly significant and plays a non-negligible role. In the yoke regions, only the tangential component of the flux density is considered. This is because the flux in the yoke is predominantly tangential, and the radial component remains negligible. In contrast, the two-component saturation correction accounting for both the radial and tangential components is applied only to the stator and rotor teeth, where the flux density is highest and the risk of deep saturation is greatest.

$$B_{r,i,tooth}^{inner\ stator} = \frac{\phi_{i,tooth}^{inner\ stator}}{L_s w_{iss} R_{iss}} \quad (24)$$

$$B_{r,i,tooth}^{outer\ stator} = \frac{\phi_{i,tooth}^{outer\ stator}}{L_s w_{oss} R_{oss}} \quad (25)$$

$$B_{\theta,i,tooth}^{yoke\ stator} = \frac{\phi_{yoke,i}^{yoke\ stator}}{L_s(R_{osy} - R_{isy})} \quad (26)$$

$$B_{r,i,tooth}^{inner\ rotor} = \frac{\phi_{i,tooth}^{inner\ rotor}}{L_s w_{irs} R_{irs}} \quad (27)$$

$$B_{r,i,tooth}^{outer\ rotor} = \frac{\phi_{i,tooth}^{outer\ rotor}}{L_s w_{ors} R_{ors}} \quad (28)$$

$$B_{\theta,yoke,i}^{inner\ rotor} = \frac{\phi_{yoke,i}^{inner\ rotorr}}{L_s(R_o - R_{ory})} \quad (29)$$

$$B_{\theta,yoke,i}^{outer\ rotor} = \frac{\phi_{yoke,i}^{outer\ rotor}}{L_s(R_{iry} - R_{shaft})} \quad (30)$$

$$B_{\theta,i,tooth}^{inner\ stator} = \frac{B_\theta^{ia}}{\mu_{r,stator}} \quad (31)$$

$$B_{\theta,i,tooth}^{outer\ stator} = \frac{B_\theta^{oa}}{\mu_{r,stator}} \quad (32)$$

$$B_{\theta,i,tooth}^{inner\ rotor} = \frac{B_\theta^{ia}}{\mu_{r,rotor}} \quad (33)$$

$$B_{\theta,i,tooth}^{outer\ rotor} = \frac{B_{\theta}^{oa}}{\mu_{r,rotor}} \quad (34)$$

3. Total Flux Density Magnitude (Two-Component Consideration)

Since saturation depends on the total flux density magnitude, both the radial and tangential components are combined in the teeth, where saturation is most likely. Equations (35) and (36) compute the total flux density magnitude in the rotor and stator teeth, respectively, covering both the inner and outer teeth. The radial component comes from the tooth flux equations, while the tangential component is derived from the continuity of the tangential magnetic field intensity at the iron–air interface. Both components must be included because, under deep saturation, the tangential component becomes non-negligible and cannot be ignored without introducing significant error into the saturation factor. In contrast, equation (37) states that in the yoke regions both stator and rotor only the tangential component is considered. The flux in the yoke is predominantly tangential.

$$\left|B_{i,tooth}^{rotor}\right| = \sqrt{{B_{r,tooth,i}}^2 + {B_{\theta,tooth,i}}^2} \quad (35)$$

$$\left|B_{i,tooth}^{stator}\right| = \sqrt{{B_{r,tooth,i}}^2 + {B_{\theta,tooth,i}}^2} \quad (36)$$

$$\left|B_{i,tooth}^{yoke}\right| = \left|B_{\theta,i,yoke}^{rotor\&stator}\right| \quad (37)$$

4. Magnetic Field Intensity from the B–H Curve

Using the actual B–H characteristic of the lamination steel as shown in Figure 6 (steel 1008), the corresponding magnetic field intensity is obtained:

$$f_{B-H}\left(\left|B_{i,tooth}^{stator}\right|\right) = \left|H_{i,tooth}^{stator}\right| \quad (38)$$

$$f_{B-H}\left(\left|B_{i,tooth}^{rotor}\right|\right) = \left|H_{i,tooth}^{rotor}\right| \quad (39)$$

$$f_{B-H}\left(\left|B_{i,yoke}^{stator\&rotor}\right|\right) = \left|H_{i,yoke}^{stator\&rotor}\right| \quad (40)$$

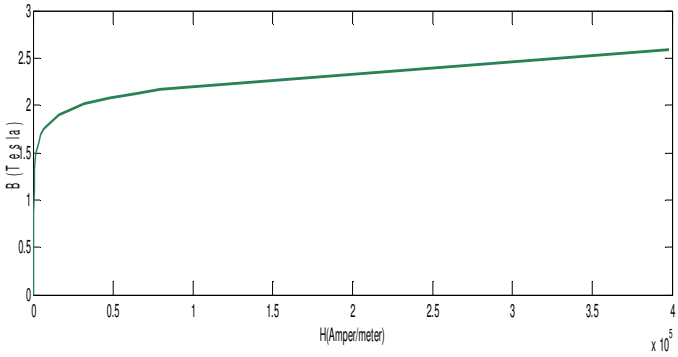


Figure. 6. Actual B-H characteristic curve for steel 1008

5. Local Saturation Factors

The saturation factors for each region are defined as:

$$k_{i,inner\ stator\ tooth}^{correction} = 1 + \frac{H_{i,tooth}^{inner\ stator}.(R_{isy} - R_{iss})}{H_{ia}.(R_{iss} - R_{irs})} \quad (41)$$

$$k_{i,inner\ rotor\ tooth}^{correction} = 1 + \frac{H_{i,tooth}^{inner\ rotor}.(R_{irs} - R_{iry})}{H_{ia}.(R_{iss} - R_{irs})} \quad (42)$$

$$k_{i,stator\ yoke}^{correction} = 1 + \frac{H_{i,tooth}^{stator\ yoke}.(\frac{\pi}{N_{iss}}.(R_{isy} + R_{osy}))}{H_{effective}^{gap}.l_{effective}} \quad (43)$$

$$k_{i,outer\ stator\ tooth}^{correction} = 1 + \frac{H_{i,tooth}^{outer\ stator}.(R_{oss} - R_{ory})}{H_{oa}.(R_{ors} - R_{oss})} \quad (44)$$

$$k_{i,outer\ rotor\ tooth}^{correction} = 1 + \frac{H_{i,tooth}^{outer\ rotor}.(R_{ory} - R_{ors})}{H_{oa}.(R_{ors} - R_{oss})} \quad (45)$$

$$k_{i,inner\ rotor\ yoke}^{correction} = 1 + \frac{H_{i,yoke}^{inner\ rotor}.(\frac{\pi}{N_{irs}}.(R_{shaft} + R_{iry}))}{H_{ia}.(R_{iss} - R_{irs})} \quad (46)$$

$$k_{i,outer\ rotor\ yoke}^{correction} = 1 + \frac{H_{i,yoke}^{outer\ rotor}.(\frac{\pi}{N_{ors}}.(R_o + R_{ory}))}{H_{oa}.(R_{ors} - R_{oss})} \quad (47)$$

$$H_{effective}^{gap} = \frac{H_{ia}.\sum_{i=1}^{N_{irs}}\phi_{i,tooth}^{inner\ rotor} + H_{oa}.\sum_{i=1}^{N_{ors}}\phi_{i,tooth}^{outer\ rotor}}{\sum_{i=1}^{N_{irs}}\phi_{i,tooth}^{inner\ rotor} + \sum_{i=1}^{N_{ors}}\phi_{i,tooth}^{outer\ rotor}} \quad (48)$$

$$l_{effective} = \frac{1}{2}.((R_{iss} - R_{iry}) + (R_{ors} - R_{oss})) \quad (49)$$

The saturation correction factors for each region are defined in equations (41) through (47), each following the same underlying principle: the correction factor is equal to unity plus the ratio of the magnetic voltage drop in the iron region to the magnetic voltage drop in the corresponding airgap. This ratio quantifies how much of the total magneto-motive force is consumed by the iron path, and therefore how much the effective airgap flux is reduced under saturation.

For the inner stator tooth and the inner rotor tooth, equations (41) and (42), the magnetic voltage drop is computed along the radial path of the tooth, while the denominator is the magnetic voltage drop across the inner airgap. The same structure applies to the outer stator tooth and the outer rotor tooth in equations (44) and (45), except that the denominator is now the magnetic voltage drop across the outer airgap.

A special case arises for the stator yoke in equation (43). Since the stator yoke in the H-Type topology is influenced by both the inner and the outer airgaps, it cannot be corrected using a single airgap. Instead, an effective airgap field intensity and an effective airgap length are introduced, which combine the contributions of both airgaps into a single representative value. These two effective quantities are defined in equations (48) and (49). The effective airgap field intensity is computed as a flux-weighted average of the inner and outer airgap field intensities, so that the airgap carrying more flux has a greater influence on the correction. The effective airgap length, in turn, is taken as the arithmetic mean of the inner and outer airgap lengths, providing a single representative length for use in the yoke correction.

For the inner rotor yoke, equation (46), the correction only involves the inner airgap, since this yoke is magnetically coupled solely to the inner side of the machine. Similarly, for the outer rotor yoke, equation (47), only the outer airgap is involved. In both cases, the effective flux path length in the yoke is expressed as the product of full the angular pitch between adjacent teeth and the mean radius of the yoke, which yields the arc length of the flux path that in Figure8, magnetic analysis is carried out to illustrate path of flux.

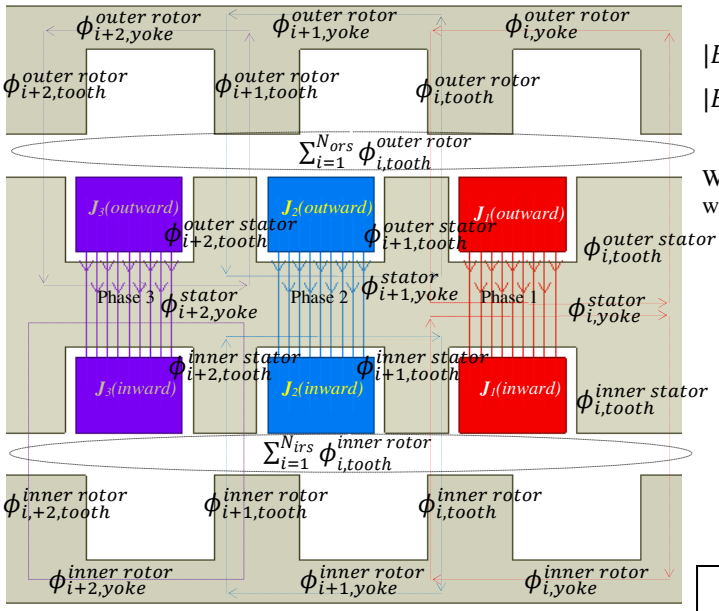


Figure 7. Flux path of proposed machine in wide view

6. Corrected Flux Density for Inner and Outer Air-gap

Equations (50) and (51) represent the final step of the saturation correction, in which the linear flux density components are corrected by dividing them by the product of the saturation factors. The radial component is corrected in equation (50), and the tangential component in equation (51), using the same set of saturation factors for the stator, rotor, and yoke.

The saturation factor $K_{correction}$ is always greater than or equal to unity and represents the fraction of the total magneto-motive force that is consumed by the iron path relative to the airgap. Since the flux must pass through the stator tooth, the rotor tooth, and the yoke to complete its magnetic circuit, the total correction is the product of the factors of all three regions. Dividing the linear flux density by this product yields the corrected, more realistic value.

$$B_{r,sat}(\theta) = \frac{B_{r,linear}(\theta)}{K_{correctin,stator}(\theta) K_{correctin,rotor}(\theta) K_{correctin,yoke}(\theta)} \quad (50)$$

$$B_{\theta,sat}(\theta) = \frac{B_{\theta,linear}(\theta)}{K_{correctin,stator}(\theta) K_{correctin,rotor}(\theta) K_{correctin,yoke}(\theta)} \quad (51)$$

7. Iterative Update

Since the saturation factors depend on the corrected flux density, the procedure is repeated iteratively:

$$B_{r_{correction},k+1}(\theta) = \frac{B_{r,linear}(\theta)}{K_{correction,stator,k}(\theta) K_{correction,rotor,k}(\theta) K_{scorrectionat,yoke,k}(\theta)} \quad (52)$$

$$B_{\theta_{correction},k+1}(\theta) = \frac{B_{\theta,linear}(\theta)}{K_{correction,stator,k}(\theta) K_{correction,rotor,k}(\theta) K_{scorrectionat,yoke,k}(\theta)} \quad (53)$$

The iteration continues until:

$$|B_{r_{correction},k+1}(\theta) - B_{r_{correction},k}(\theta)| < \varepsilon \quad (54)$$

$$|B_{\theta_{correction},k+1}(\theta) - B_{\theta_{correction},k}(\theta)| < \varepsilon \quad (55)$$

Where ε is typically set to 1%. Typically, convergence is achieved within 4–6 iterations. Whole processes are embedded in Figure8.

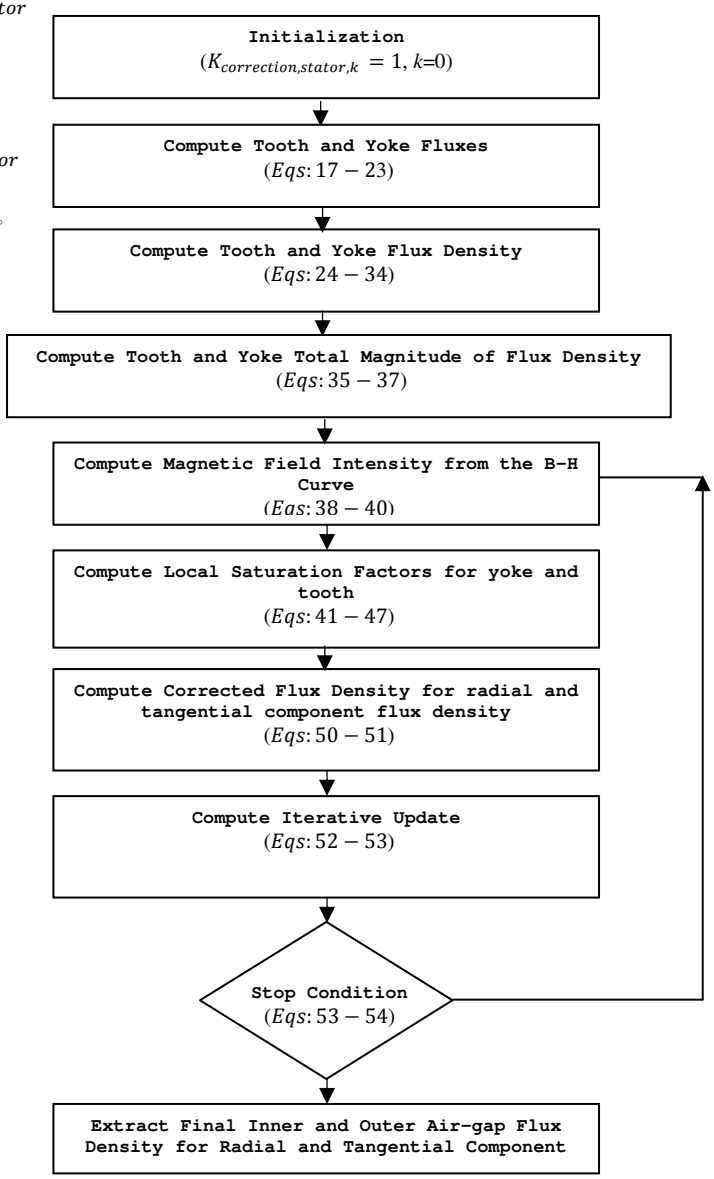


Figure 8. Flow chart of Two-Component Saturation Correction method

8. Electromagnetic Quantities

Once the corrected field solution is obtained, the key electromagnetic quantities are computed.

The tangential stress acting on the rotor surface is:

$$f_\theta = \frac{B_r B_\theta}{\mu_0} \tag{56}$$

The total torque is obtained by integrating this stress over the rotor surface that R is the radius of calculated flux density in inner and outer air gap:

$$T_{ele} = R^2 . L_s \int_0^{2\pi} f_\theta d\theta \tag{57}$$

The radial stress components are:

$$f_r = \frac{({B_r}^2 - {B_\theta}^2)}{2\mu_0} \tag{58}$$

The resultant UMF is:

$$F_{UMF} = \sqrt{{F_x}^2 + {F_y}^2} \tag{59}$$

Where:

$$F_x = R . L_s \int_0^{2\pi} (f_r \cos(\theta) - f_\theta \sin(\theta))\, d\theta \tag{60}$$

$$F_y = R . L_s \int_0^{2\pi} (f_r \sin(\theta) + f_\theta \cos(\theta)) d\theta \tag{61}$$

III. Results And Validation

To evaluate the accuracy and effectiveness of the proposed analytical model, three sets of results are compared: the linear analytical model (infinite permeability assumption), the nonlinear analytical model (with the two-component saturation correction), and the finite element method (FEM), which serves as the reference. The simulations are carried out at the rated current density of 36 A/mm², which is deliberately chosen to push the iron core into deep saturation, particularly in the stator and rotor teeth, where the flux density exceeds the knee point of the *B–H* curve. This provides a rigorous test case for assessing the capability of the proposed saturation correction technique. Since the inner and outer stator slots have different cross-sectional areas, two separate filling factors, k_{fi} and k_{fo}, are defined for the inner and outer slots, respectively. The inner and outer windings are connected in series, so the same phase current flows through both. The use of two distinct filling factors ensures that the current density in each slot remains consistent with its geometry, and allows the model to be generalized to arbitrary slot dimensions.

The machine dimensions used for validation are listed in Table 1. These parameters correspond to the prototype geometry of the proposed H-Type SRM and are applied consistently in the analytical model, the FEM model, and the linear model simulations. Figure 9 illustrates the details of the validation model, including the machine geometry, the winding arrangement, and the initial rotor position at time t=0(s). The phase currents are determined by the three-phase excitation described in equations (62)–(64), which define the current density in the three phases as a function of time. Since the inner and outer parts share the same number of rotor slots ($N_{irs} = N_{ors}$), the same excitation pattern applies to both.

It should be noted that the comparison of the radial and tangential flux density components, as well as the radial pressure distribution, is carried out at time t=0 (s) and at the initial rotor position of 0°, for both the inner and outer structures. In contrast, the remaining results namely the electromagnetic torque and the unbalanced magnetic UMF are obtained by rotating the rotor, so that the variation of these quantities with rotor position can be properly captured and compared.

$$J_a(t) = k_f J_m sin\,(N_{irs}\omega_m t) \tag{62}$$

$$J_b(t) = k_f J_m sin\,(N_{irs}\omega_m t + \frac{2\pi}{3}) \tag{63}$$

$$J_c(t) = k_f J_m sin\,(N_{irs}\omega_m t - \frac{2\pi}{3}) \tag{64}$$

Where J_m is the peak current density, ω_m is the mechanical angular frequency. At t=0(s), the current densities in the three phases are J_a= 0 (A/mm²), $J_b = +\frac{\sqrt{3}}{2} k_f J_m$ (A/mm²), and $J_C = -\frac{\sqrt{3}}{2} k_f J_m$ (A/mm²) corresponding to a balanced three-phase excitation. This initial condition is used consistently in both the analytical model and the FEM simulations to ensure a fair comparison.

Table 1. Geometry of H-Type SRM for modeling

Parameters	Value
Maximum current density of inner winding, J_i	36A/mm²
Maximum current density of outer winding, J_o	36A/mm²
Number of inner stator slots, N_{iss}	12
Number of outer stator slots, N_{oss}	12
Number of inner phases, N_{iph}	3
Number of outer phases, N_{oph}	3
Number of inner rotor slots, N_{irs}	10
Number of outer rotor slots, N_{ors}	10
Width of inner rotor slot, w_{irs}	26.99 π/180 rad
Width of outer rotor slot, w_{ors}	27.01π/180 rad
Width of inner stator slot, w_{iss}	12.5 π/180 rad
Width of outer stator slot, w_{oss}	6.92 π/180 rad
Inner rotor yoke radius, R_{iry}	26mm
Outer rotor yoke radius, R_{ory}	102mm
Inner stator yoke radius, R_{isy}	60mm
Outer stator yoke radius, R_{osy}	75mm
Inner radius of inner stator, R_{iss}	38mm
Outer radius of outer stator, R_{oss}	92.09mm
Inner radius of outer rotor, R_{ors}	93.5mm
Outer radius of inner rotor, R_{irs}	37mm
Radius of rotor shaft, R_{shaft}	10mm
Outer radius of rotor, R_o	120mm
Stack length, L_s	100mm
Filling factor outer stator slot, K_{fi}	1
Filling factor inner stator slot, K_{fo}	0.7
Inner rotor speed, ω_m	62.83 rad/s
Outer rotor speed, ω_m	62.83 rad/s

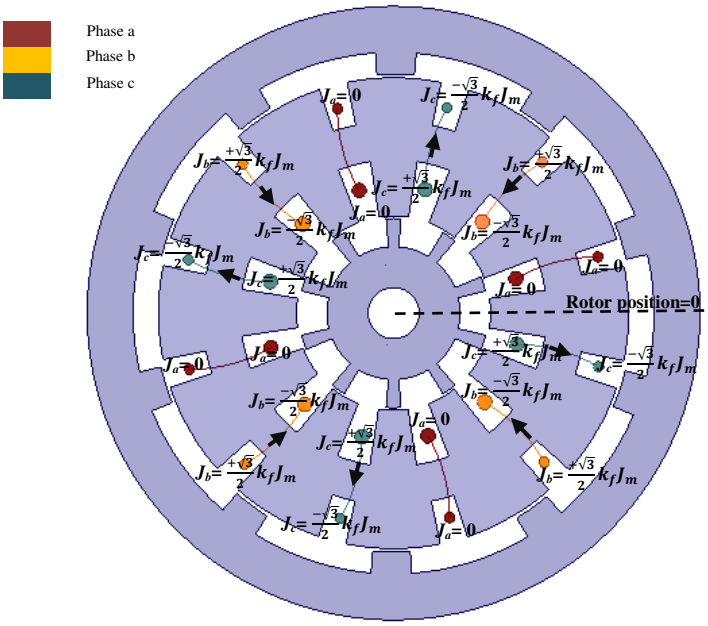


Figure 9. Geometry of H-type SRM at t=0(s) and rotor position of 0°

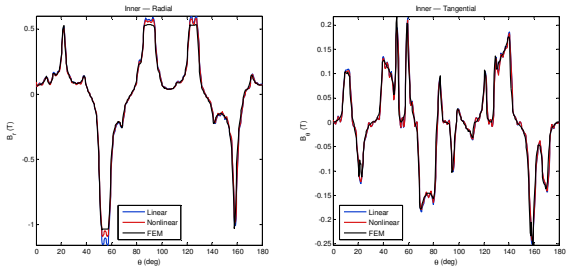


Figure 10. Radial and tangential components of the airgap flux density for the inner structure: comparison between FEM, linear analytical model, and nonlinear analytical model.

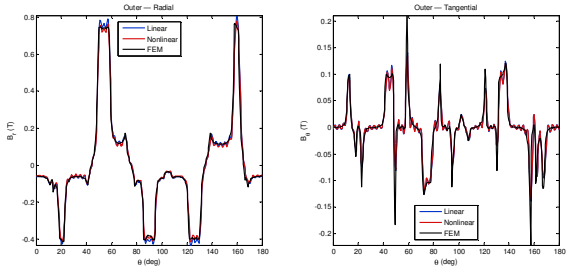


Figure 11. Radial and tangential components of the airgap flux density for the outer structure: comparison between FEM, linear analytical model, and nonlinear analytical model.

As shown in Figure 10, the nonlinear model gives a better prediction of the flux density in the saturated regions, particularly near the tooth tips, where the linear model shows more deviation from FEM. The nonlinear results follow the FEM waveform and amplitude more closely, which indicates that the two-component saturation correction improves the modeling of the iron core nonlinear behavior in the inner structure. A similar improvement is observed for the outer structure in Figure 11, where the nonlinear model again provides results closer to FEM than the linear model. This consistent improvement for both the inner and outer structures shows the generality of the proposed approach.

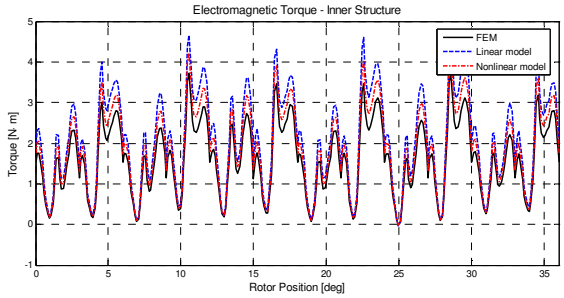


Figure 12. Electromagnetic torque for the inner structure as a function of rotor position and time: comparison between FEM, linear analytical model, and nonlinear analytical model.

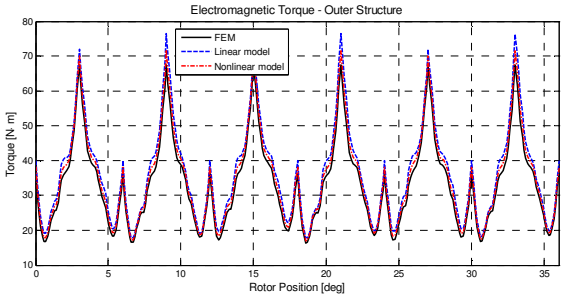


Figure 13. Electromagnetic torque for the outer structure as a function of rotor position and time: comparison between FEM, linear analytical model, and nonlinear analytical model.

Figure 12 shows the electromagnetic torque for the inner structure. The nonlinear model provides a better prediction of the torque waveform compared with the linear model, and the ripple content is reproduced more closely to the FEM result. In contrast, the linear model shows larger deviation in both the average torque and the ripple. This indicates that the saturation correction improves the accuracy of torque prediction. A similar improvement is observed for the outer structure in Figure 13, where the nonlinear model again gives results closer to FEM, while the linear model exhibits more noticeable deviation. The torque ripple is also better captured by the nonlinear model, which is important for applications requiring smooth torque production.

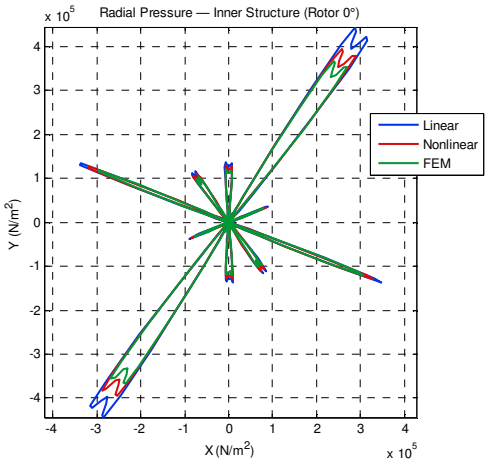


Figure 14. Radial pressure distribution for the inner structure at the initial rotor position: comparison between FEM, linear analytical model, and nonlinear analytical model.

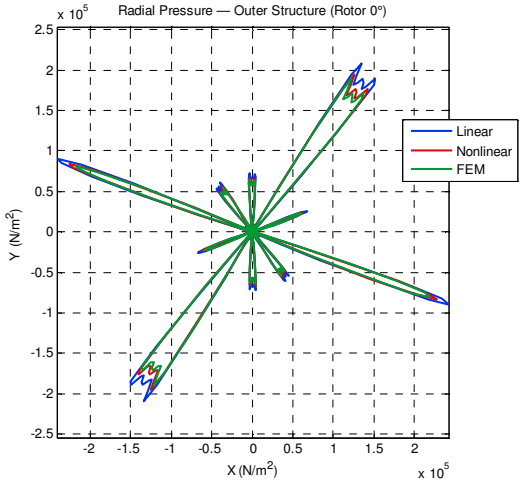


Figure 15. Radial pressure distribution for the outer structure at the initial rotor position: comparison between FEM, linear analytical model, and nonlinear analytical model.

Figure 14 shows the radial pressure distribution for the inner structure at the initial rotor position. Radial pressure is a critical parameter for bearingless applications, since it directly determines the magnetic suspension force and, consequently, the stability of rotor levitation. The nonlinear model provides a better prediction of the radial pressure compared with the linear model and follows the FEM result more closely, whereas the linear model shows larger deviation in the saturated regions. Such deviation is undesirable for bearingless systems, because it may mislead the suspension controller into assuming more radial force is available than actually exists. As shown in Figure 15, a similar improvement is observed for the outer structure, indicating that the saturation correction enhances the accuracy for both sides of the machine.

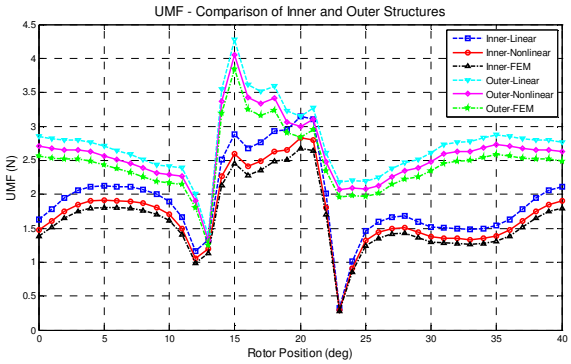


Figure 16. UMF for the inner and outer structure as a function of rotor position with excitation at t=0 (s): comparison between FEM, linear analytical model, and nonlinear analytical model.

Figure 16 shows the UMF for the inner and outer structure as a function of rotor position. The UMF is computed from both the radial and tangential stress components, using equations (56)–(61). The nonlinear model provides a better prediction of the UMF magnitude and waveform compared with the linear model, which shows larger deviation in the saturated regions. Improved UMF prediction is important for vibration and acoustic noise analysis, as well as for bearing and rotor support design. Taken together, the results presented in Figures 10–16 show that the proposed nonlinear analytical model, with the two-component saturation correction, improves the reproduction of the field distribution and the integral quantities of the H-Type SRM, while offering a significant reduction in computational time compared to FEM.

IV. Discussion

The results presented in previous section demonstrate that the proposed nonlinear analytical model, incorporating the two-component saturation correction, provides a marked improvement over the conventional linear model in predicting the electromagnetic behavior of the H-Type SRM. This section discusses the key observations, their physical interpretation, and the implications for design and analysis.

A. Field Distribution and Saturation Effect

The comparison of the airgap flux density in Figures 10 and 11 reveals that the linear model significantly overestimates the radial and tangential components in the saturated regions, particularly near the tooth tips and pole edges. This overestimation is a direct consequence of assuming infinite permeability in the iron core, which neglects the reduction of effective permeability under high flux density. In contrast, the nonlinear model, by iteratively updating the local saturation factors based on the actual B–H curve, follows the FEM waveform and amplitude much more closely. The improvement is consistent for both the inner and outer structures, confirming the generality of the proposed approach.

A key observation is that the tangential component of the flux density, often neglected in conventional analytical models, plays a non-negligible role under deep saturation. As shown in Figures 10 and 11, the tangential component reaches values comparable to the radial component in certain angular regions, and its accurate prediction is essential for the correct estimation of both torque and UMF.

B. Electromagnetic Torque

Figures 12 and 13 compare the electromagnetic torque predicted by the linear and nonlinear models with the FEM reference for the inner and outer structures, respectively. The nonlinear model reproduces electromagnetic torque more accurately than the linear model. A summary of the torque comparison is provided in Table II.

Table II. Comparison of electromagnetic torque (inner and outer structures)

Quantity	Linear	Nonlinear	FEM
Average torque -inner (N·m)	~2.1	~1.8	~1.6
Average torque -outer (N·m)	~42.5	~38.2	~36.4

The improved torque prediction is attributed to the corrected flux density in the teeth and yoke, which directly affects the tangential stress and hence the torque integral in Eq. (57).

C. Radial Pressure and UMF

Figures 14 and 15 show the radial pressure distribution at the initial rotor position for the inner and outer structures. Radial pressure is a critical parameter for bearingless applications, as it determines the magnetic suspension force and the stability of rotor levitation. The nonlinear model follows the FEM result more closely than the linear model, especially in the saturated regions.

Figure 16 presents the UMF as a function of rotor position for both structures. The UMF is computed from both radial and tangential stress components using Eqs. (56)–(61). The nonlinear model provides a better prediction of both the magnitude and waveform of the UMF, particularly in the angular regions where saturation is most pronounced. Accurate UMF prediction is essential for vibration and acoustic noise analysis, as well as for the mechanical design of the rotor support and bearings. A quantitative comparison is summarized in Table III.

Table III. Comparison of radial pressure and UMF (inner and outer structures)

Quantity	Linear	Nonlinear	FEM
Peak radial pressure - inner (N/m²)	~5.2×10^5	~4.6×10^5	~4.45×10^5
Peak radial pressure -outer (N/m²)	~2.1×10^5	~1.85×10^5	~1.78×10^5
Peak UMF - inner (N)	~3.2	~2.8	~2.6
Peak UMF - outer (N)	~4.3	~4.05	~3.95
Average UMF - inner (N)	~2.45	~2.05	~1.95
Average UMF - outer (N)	~3.1	~3	~2.9

D. Computational Efficiency

One of the main advantages of the proposed analytical model is its computational efficiency. While a full 3D FEM simulation of the H-Type SRM may require several hours, the proposed analytical model converges within a few seconds on a standard desktop computer, with the iterative saturation correction typically converging in 4–6 iterations. This makes the model particularly suitable for design optimization, parametric studies, and real-time control applications where repeated evaluation of the electromagnetic performance is required. A comparison of computation times is presented in Table IV.

Table IV. Comparison of computation time

Method	Computation time (s)	Relative speed
FEM	~600	-
Linear analytical	~15	40× faster
Nonlinear analytical	~20	30× faster

V. Conclusion

This paper has presented a two-dimensional analytical subdomain model for an H-Type switched reluctance machine with a circumferential cross-winding arrangement, incorporating an iterative two-component saturation correction. The model accounts for both radial and tangential flux density components and is validated against finite element simulations for the inner and outer structures of the machine.

The main findings of this work are summarized as follows:

1. **Improved accuracy under saturation:** The nonlinear model significantly reduces the error in flux density, torque, radial pressure, and UMF compared with the conventional linear model, particularly in the saturated regions near the tooth tips.
2. **Role of the tangential component:** Under deep saturation, the tangential component of the flux density becomes non-negligible and must be included for accurate prediction of torque and UMF.
3. **Computational efficiency:** The proposed model converges within a few seconds, offering a substantial reduction in computation time compared with FEM while maintaining acceptable accuracy.
4. **Applicability to bearingless systems:** The model provides reliable estimates of radial pressure and UMF, which are essential for stable rotor levitation in bearingless applications.

In conclusion, the proposed framework offers a reliable, accurate, and computationally efficient tool for the analysis and design of H-Type SRM topologies, with particular relevance to in-wheel traction drives and high-speed actuator systems.

Author contributions

E.S. conceptualized the study, developed the mathematical framework based on the subdomain method, derived the analytical solutions, and carried out the theoretical analysis. E.S. contributed to the analytical modeling, finite element analysis (FEA) simulations, validation of the results, and the sensitivity analysis for cogging torque minimization. The author wrote and reviewed the manuscript. The author read and approved the final manuscript.

Declarations

Ethical approval: Not applicable.

Consent to participate: Not applicable.

Consent to publish: Not applicable.

Data availability: The datasets generated and/or analyzed during the current study are available from the corresponding author on reasonable request. All numerical results were obtained from analytical modeling and finite element simulations using the mathematical models, formulations, and parameter values reported in this article.

Competing interests: The author declares no competing interests.

Funding: The author received no specific funding for this work.

REFERENCES

[1] B. Fahimi, A. Emadi, and R. B. Sepe, "A switched reluctance machine-based starter/alternator for more electric cars," *IEEE Trans. Energy Convers.*, vol. 19, no. 1, pp. 116–124, Mar. 2004.

[2] Y. Hu et al., "New SR drive with integrated charging capacity for plug-in hybrid electric vehicles (PHEVs)," *IEEE Trans. Ind. Electron.*, vol. 61, no. 10, pp. 5722–5731, Oct. 2014.

[3] W. Hua et al., "Comparative study of switched reluctance machines with half- and full-teeth-wound windings," *IEEE Trans. Ind. Electron.*, vol. 63, no. 3, pp. 1414–1424, Mar. 2016.

[4] A. Vadde and S. Sachin, "Unitized double sided linear switched reluctance motor with auxiliary winding for rope less elevators," in *Proc. 2024 Third Int. Conf. Power, Control and Computing Technologies (ICPC2T)*, Raipur, India, Jan. 18–20, 2024. doi: 10.1109/ICPC2T60072.2024.10474772.

[5] J. Parmar, J. Panchal, T. Jhankal, and A. N. Patel, "Selection of stator pole tip for torque ripple reduction of switched reluctance motor," in *Proc. 2024 IEEE 11th Power India International Conference (PIICON)*, Jaipur, India, Dec. 10–12, 2024. doi: 10.1109/PIICON63519.2024.10995057.

[6] R. R. Caicedo Castro, V. A. de Abreu Batista, R. G. Intriago-Velasquez, B. Aderbal De Oliveira, M. V. De Paula, and T. A. dos S. Barros, "Comparative analysis of winding configurations in a 16/12 switched reluctance motor," in *Proc. 2025 Brazilian Power Electronics Conference (COBEP)*, Vitoria, Brazil, Oct. 5–8, 2025. doi: 10.1109/COBEP66423.2025.11231659.

[7] I. Verbytskyi, V. Zhuikov, and O. Abakumova, "Mathematical model of switched reluctance motor for braking force elimination," in *Proc. 2024 IEEE 7th Int. Conf. Smart Technologies in Power Engineering and Electronics (STEE)*, Kyiv, Ukraine, Sep. 24–26, 2024. doi: 10.1109/STEE63556.2024.10747819.

[8] Z. Xu, C. Huang, S. Yu, H. Wang, T. Yi, and Z. Zhang, "Mathematical model of 12/14 hybrid stator pole type bearingless switched reluctance motor based on Maxwell stress tensor method," in *Proc. 2022 IEEE 5th Int. Electrical and Energy Conference (CIEEC)*, Nanjing, China, May 27–29, 2022. doi: 10.1109/CIEEC54735.2022.9845864.

[9] D. Fu, Z. Lv, H. Si, Y. Liu, and X. Wu, "Analysis and comparison of novel yokeless double rotor mutually coupled switched reluctance motor," in *Proc. 2023 IEEE Int. Magnetic Conference - Short Papers (INTERMAG Short Papers)*, Sendai, Japan, May 15–19, 2023. doi: 10.1109/INTERMAGShortPapers58606.2023.10228424.

[10] Z. Xu, Q. Yu, and F. Zhang, "Design and analysis of asymmetric rotor pole type bearingless switched reluctance motor," *CES Trans. Electrical Machines and Systems*, vol. 6, no. 1, pp. 3–10, Mar. 2022. doi: 10.30941/CESTEMS.2022.00002.

[11] Z. Rayeen and S. Payami, "Analytical modeling and optimization of an outer rotor-five phase switched reluctance motor for in-wheel drive applications," in *Proc. 2023 IEEE Int. Transportation Electrification Conference (ITEC-India)*, Chennai, India, Dec. 12–15, 2023. doi: 10.1109/ITEC-India59098.2023.10471424.

[12] S. Das, D. Roy, and M. Sengupta, "Detailed FEM-based analysis of vibration in a 3-phase switched reluctance motor and its experimental validation," in *Proc. 2022 IEEE Int. Conf. Signal Processing, Informatics, Communication and Energy Systems (SPICES)*, Thiruvananthapuram, India, Mar. 10–12, 2022. doi: 10.1109/SPICES52834.2022.9774166.

[13] R. Kokubu and K. Kiyota, "Performance balancing design method for 12-pole 20-slot five-phase multi-mode reluctance motor," in *Proc. 2025 IEEE Energy Conversion Congress and Exposition (ECCE)*, Philadelphia, PA, USA, Oct. 19–23, 2025. doi: 10.1109/ECCE58356.2025.11260138.

[14] D. Roy and M. Sengupta, "An experimentally validated novel analytical approach for modeling of a saturated switched reluctance motor," *IEEE Trans. Magnetics*, vol. 58, no. 12, Art. no. 8207011, Dec. 2022. doi: 10.1109/TMAG.2022.3210155.

[15] K. Diao, X. Sun, G. Bramerdorfer, G. Li, Q. Wang, and L. Wu, "A novel analytical design theory for switched reluctance motors incorporating nonlinear characteristics," *IEEE Trans. Industrial Electronics*, vol. 72, no. 7, pp. 6775–6785, Jul. 2025. doi: 10.1109/TIE.2024.3511123.

[16] T. Kusumi, K. Kobayashi, K. Umetani, and E. Hiraki, "Analytical derivation of phase-current waveform for elimination of torque and input-current ripples of switched reluctance motor operating under magnetic saturation," *IEEE Trans. Industry*

Applications, vol. 58, no. 4, pp. 5248–5261, Jul.–Aug. 2022. doi: 10.1109/TIA.2022.3172898.

[17] Z. Rayeen and S. Payami, "Design methodology and analytical model for higher phase switched reluctance motor considering mutual coupling and saturation effect," *IEEE Trans. Industrial Electronics*, vol. 72, no. 12, pp. 12016–12027, Dec. 2025. doi: 10.1109/TIE.2025.3569973.

[18] M. I. Elkasas, A. L. Saleh, A. Ghanem, M. F. Kotb, and M. Hamouda, "Magnetic characterization-based modeling of switched reluctance motors considering interturn short circuit faults," *IEEE Access*, vol. 13, pp. 185570–185584, 2025. doi: 10.1109/ACCESS.2025.3624075.

[19] G. Watthewaduge and B. Bilgin, "Reluctance mesh-based magnetic equivalent circuit modeling of switched reluctance motors for static and dynamic analysis," *IEEE Trans. Transportation Electrification*, vol. 8, no. 2, pp. 2164–2176, Jun. 2022. doi: 10.1109/TTE.2021.3132885.

[20] Z. Li, D. Wang, C. Huang, S. Xu, and X. Wang, "Nonlinear analytical model of linear switched reluctance motor with segmented secondary considering iron saturation and end effect," *IEEE Access*, vol. 11, pp. 132078–132087, 2023. doi: 10.1109/ACCESS.2023.3335811.

[21] Z. Wang, X. Cao, Z. Deng, and J. Cai, "Electromagnetic modeling and investigation for bearingless switched reluctance motor considering magnetic saturation," *IEEE Trans. Energy Conversion*, vol. 38, no. 1, pp. 122–133, Mar. 2023. doi: 10.1109/TEC.2022.3208831.

[22] F. Yu, H. Chen, W. Yan, D. Zhou, X. Wang, and Y. Gorbounov, "Performance improvement for double-stator axial flux SRM using a new winding reconfigurable power converter," *IEEE Trans. Transportation Electrification*, vol. 9, no. 2, pp. 3295–3307, Jun. 2023. doi: 10.1109/TTE.2022.3228913.

[23] S. Oncu, U. Tuncer, and S. Koyuncu, "Modeling and simulation of external rotor 6/8 switched reluctance motor for e-bike," in *Proc. 2022 10th Int. Conf. Smart Grid (icSmartGrid)*, Istanbul, Turkey, Jun. 27–29, 2022. doi: 10.1109/icSmartGrid55722.2022.9848688.

[24] J. Sun, Y. Yang, C. Gan, et al., "Analytical inductance modeling of segmental rotor switched reluctance motor with single-tooth windings," *J. Electr. Eng. Technol.*, vol. 19, pp. 3283–3295, 2024. doi: 10.1007/s42835-024-01800-3.

[25] G. Zhang, W. Zhang, P. Zhang, et al., "Investigation on modulating behaviors of reluctance motors based on air-gap field modulation theory," *J. Electr. Eng. Technol.*, 2026. doi: 10.1007/s42835-026-02927-1.

[26] A. Dahane, F. Z. El mansouri, A. Brouri, H. Oubbouaddi, M. I. Mosaad, and L. Kadi, "Nonlinear modeling and electromagnetic parameters identification for switched reluctance machine," in *Proc. Int. Conf. Advanced Communications with Modern Circuits and Systems Technologies (ACMCST 2025)*, Lecture Notes in Networks and Systems, vol. 1852, M. Saih, A. Reha, and Y. Lakhal, Eds. Cham, Switzerland: Springer, 2026. doi: 10.1007/978-3-032-18857-1_24.

[27] E. F. Farahani, N. J. Baker, and F. Mahmouditabar, "An innovative H-type flux switching permanent magnet linear generator for thrust force enhancement," *Energies*, vol. 16, no. 16, Art. no. 5976, 2023. doi: 10.3390/en16165976.